


One-dimensional quantum spin dynamics of Bethe string statesWang Yang,¹ Jianda Wu,^{1,*} Shenglong Xu,¹ Zhe Wang,² and Congjun Wu^{1,†}¹*Department of Physics, University of California, San Diego, California 92093, USA*²*Experimental Physics V, Center for Electronic Correlations and Magnetism, Institute of Physics, University of Augsburg, 86135 Augsburg, Germany* (Received 14 July 2016; revised manuscript received 7 September 2019; published 6 November 2019)

Quantum dynamics of strongly correlated systems is a challenging problem. Although the low energy fractional excitations of one-dimensional integrable models are often well understood, exploring quantum dynamics in these systems remains challenging in the gapless regime, especially at intermediate and high energies. Based on the algebraic Bethe ansatz formalism, we study spin dynamics in a representative one-dimensional strongly correlated model, i.e., the antiferromagnetic spin- $\frac{1}{2}$ XXZ chain with the Ising anisotropy, via the form-factor formulas. Various excitations at different energy scales are identified crucial to the dynamic spin structure factors under the guidance of sum rules. At small magnetic polarizations, gapless excitations dominate the low energy spin dynamics arising from the magnetic-field-induced incommensurability. In contrast, spin dynamics at intermediate and high energies is characterized by the two- and three-string states, which are multiparticle excitations based on the commensurate Néel ordered background. Our work is helpful for experimental studies on spin dynamics in both condensed matter and cold atom systems beyond the low energy effective Luttinger liquid theory. Based on an intuitive physical picture, we speculate that the dynamic feature at high energies due to the multiparticle antibound state excitations can be generalized to nonintegrable spin systems.

DOI: [10.1103/PhysRevB.100.184406](https://doi.org/10.1103/PhysRevB.100.184406)**I. INTRODUCTION**

The real-time dynamics reveals rich information of the quantum nature of strongly correlated many-body states [1–14]. On the other hand, one-dimensional integrable models due to their exact solvability provide reliable reference points for studying quantum and thermodynamic correlations [15–27], and certain characteristic features exhibited in these integrable models are relevant to even nonintegrable systems. The spin- $\frac{1}{2}$ antiferromagnetic (AFM) Heisenberg XXZ chain, a representative of integrable models, is an ideal system for a nonperturbative study on quantum spin dynamics [28–37]. Nevertheless, it remains a very challenging problem due to the interplay between quantum fluctuations and the dynamic evolution. On the experimental side, a great deal of high precision measurements have been performed on quasi-one-dimensional (1D) materials by using neutron scattering and electron spin resonance (ESR) spectroscopy [12,38–47]. These systems are faithfully described by the 1D spin- $\frac{1}{2}$ AFM Heisenberg model.

There has appeared significant progress in calculating the dynamic spin structure factors (DSSF) [28–36]. At zero field, contributions to the DSSFs from the two- and four-spinon excitations can be calculated analytically by using the quantum affine symmetry [48–52], however, this method ceases to apply at nonzero fields. In the algebraic Bethe ansatz

formalism [18,53], the matrix elements of local spin operators between two different Bethe eigenstates are expressed in terms of the determinant formulas in finite systems [54–57]. Accompanied with a judicious identification of the dominant excitations to spin dynamics, this method can be used to efficiently calculate the DSSFs for considerably large systems. Excellent agreements between theories and experiments have been established for the SU(2) invariant spin- $\frac{1}{2}$ AFM Heisenberg chain, confirming the important role of spinon excitations in the dynamic properties [46].

In this paper, we study quantum spin dynamics in an AFM spin- $\frac{1}{2}$ XXZ chain with the Ising anisotropy at zero temperature in a longitudinal magnetic field. The spin chain under consideration is gapped at zero field, and an increasing field tunes the system into the gapless regime [17], in which the full spin dynamics remains to be explored. Working within the algebraic Bethe ansatz formalism, we identify various spin excitations separated at different energy scales. The $S^{+-}(q, \omega)$ channel is dominated by the spinon pair excitations resembling the zero field des Cloizeaux-Pearson (DCP) modes [58], whose momentum range shrinks with increasing polarization. The coherent low energy excitations of the $S^{+-}(q, \omega)$ channel resemble the Larmor mode at $q \rightarrow 0$ and become incoherent at $q \rightarrow \pi$. The two- and three-string states play important roles at intermediate and high energies, reflecting the background Néel configuration. The low energy excitations in the longitudinal $S^{zz}(q, \omega)$ channel exhibit the soundlike spectra at $q \rightarrow 0$ while the spectra in the high energy sector reflect the excitonic excitations on the gapped Néel background. These high-frequency features of spin dynamics cannot be captured

*wjdandstein@gmail.com

†wucj@physics.ucsd.edu

by the low energy effective Luttinger liquid theory. Based on a simple physical picture, we argue that the revealed dynamic features are also relevant to nonintegrable cases.

The rest of this paper is organized as follows. In Sec. II, the model Hamiltonian is presented. In Sec. III, the method of algebraic Bethe ansatz and the calculation method are introduced. In Sec. IV, the transverse DSSFs are calculated. In Sec. V, the longitudinal DSSFs are calculated. Discussions and conclusions are made in Sec. VI. Various details of calculations are presented in Appendices A–F.

II. THE MODEL HAMILTONIAN

The Hamiltonian of the 1D spin- $\frac{1}{2}$ AFM chain with the periodic boundary condition in the longitudinal magnetic field h is defined as

$$H_0 = J \sum_{n=1}^N \left\{ S_n^x S_{n+1}^x + S_n^y S_{n+1}^y + \Delta \left(S_n^z S_{n+1}^z - \frac{1}{4} \right) \right\},$$

$$H = H_0 - h \sum_{n=1}^N S_n^z, \quad (1)$$

where N is the total site number. The spin operators on the n th site are $S_n^\alpha = \frac{1}{2} \sigma^\alpha$ with $\alpha = x, y, z$. We consider the axial region with the anisotropic parameter $\Delta = \cosh \eta > 1$.

The ground state at zero field is known to exhibit the long-range Neel ordering, and, hence, is spin gapped. If the external field h is small, then there is no magnetization. The magnetization $m = \langle G | S_T^z | G \rangle / N$ starts to develop when h is above a critical value $h_c(\Delta)$, and then the system enters the gapless regime, where $|G\rangle$ represents the ground state and $S_T^z = \sum_{i=1}^N S_i^z$ is the z component of total spin. h and m are conjugate variables through the relation $h = \partial e_0 / \partial m$ with $e_0 = \langle G | H_0 | G \rangle / N$. For calculations presented below, we adopt a typical value of $\Delta = 2$ (which applies to the SrCo₂V₂O₈ material [59]) and $N = 200$ unless explicitly mentioned, and the corresponding critical field is $h_c/J = 0.39$ [17]. We will calculate the zero temperature DSSFs, which are expressed in the Lehman representation as

$$S^{a\bar{a}}(q, \omega) = 2\pi \sum_{\mu} |\langle \mu | S_q^{\bar{a}} | G \rangle|^2 \delta(\omega - E_\mu + E_G), \quad (2)$$

where $a = \pm$ and z ; $\bar{a} = -a$ for $a = \pm$, and $a = \bar{a}$ for $a = z$; $S_i^\pm = \frac{1}{\sqrt{2}}(S_x \pm iS_y)$ and the Fourier component of spin is defined as

$$S_q^a = \frac{1}{\sqrt{N}} \sum_j e^{iqj} S_j^a, \quad (3)$$

$|\mu\rangle$ is the complete set of eigenstates; E_G and E_μ are eigenenergies of the ground and excited states, respectively.

III. THE BETHE ANSATZ METHOD

In this section, we briefly describe the Bethe ansatz method that we employ to calculate the DSSF. The fully polarized state with all spins up is taken as the reference state, based on which the flipped spins are viewed as particles. A state with M flipped spins is denoted an M -particle state and the

polarization $m = 1/2 - M/N$. Each particle wave vector k_j is related to a rapidity λ_j through the relation

$$e^{ik_j} = \sin\left(\lambda_j + i\frac{\eta}{2}\right) / \sin\left(\lambda_j - i\frac{\eta}{2}\right). \quad (4)$$

The set of rapidities $\{\lambda_j\}_{1 \leq j \leq M}$ are determined by the integer- or half-integer-valued Bethe quantum numbers I_j as presented in Appendix A. The ‘‘psinon’’-pair states $n\psi\psi$ and ‘‘psinon-antipsinon’’ pair states $n\psi\psi^*$ ($n = 1, 2$) with n the pair number play important roles in both transverse and longitudinal DSSFs. These eigenstates possess real rapidities [32,60] and their Bethe quantum numbers are presented in Appendix A.

If some λ_j 's are complex [15], the corresponding states are termed as string states [20] in which some particles form bounded excitations as discussed in Appendix B. The string ansatz is an approximation assuming the string pattern of the complex rapidity distribution. A length- l ($l \geq 1$) string is denoted as $\chi^{(l)}$, which represents a set of complex rapidities

$$\lambda_j^{(l)} = \lambda^{(l)} + i\frac{\eta}{2}(l + 1 - 2j), \quad (5)$$

for $1 \leq j \leq l$. Their common real part $\lambda^{(n)}$, the string center, is determined from the Bethe-Gaudin-Takahashi (BGT) equations with the reduced Bethe quantum numbers [20] shown in Appendix B.

Below we only consider the solutions with one length- l string denoted as $1\chi^{(l)}R$ where $R = m\psi\psi^*$ or $m\psi\psi$. The errors of complex rapidities are used to judge the validity of the string ansatz, which can be analytically checked [61]. For the calculated range of $2m$ from 0.1 to 0.9, our results exhibit a high numeric accuracy. A bar of 10^{-6} is set and only string states within this bar are kept in calculating DSSFs. The detailed discussions on the error estimation and how to systematically improve the string ansatz in an exact manner are included in Appendix D.

The determinant formulas for the form factors $\langle \mu | S_j^\pm | G \rangle$ can be obtained from the rapidities as presented in Ref. [57] and as summarized in Appendix C. Due to the exponentially large number of excited states, only a subset of them with dominating contributions to the DSSFs are selected. The validity of the selection is checked by comparing the results with the exact sum rules, and these sum rules are derived in Appendix E.

IV. THE TRANSVERSE DYNAMIC SPIN STRUCTURE FACTOR

In this section, we discuss the dominant contributions of excited states to the transverse DSSFs including $n\psi\psi^*$, $n\psi\psi$ ($n = 1, 2$), $1\chi^{(2)}R$, and $1\chi^{(3)}R$ where $R = 1\psi\psi^*$ and $1\psi\psi$. We also check the saturation of these excitations by comparing with the exact sum rules.

A. The momentum-resolved sum rule of the transverse DSSF

The transverse first frequency moment (FFM) sum rule is

$$W_\perp(q) = \int_0^\infty \frac{d\omega}{2\pi} \omega [S^{+-}(q, \omega) + S^{-+}(q, \omega)]$$

$$= \alpha_\perp + \beta_\perp \cos q, \quad (6)$$

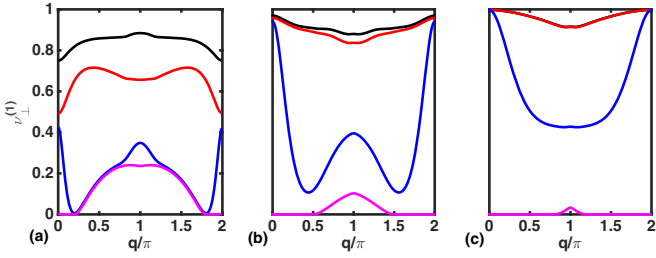


FIG. 1. The momentum-resolved FFM ratios with $2m$ equal to (a) 0.2, (b) 0.5, and (c) 0.8, respectively. The pink, blue, red, and black curves represent cumulative results by including the psinon states $n\psi\psi$ ($n = 1, 2$) in S^{-+} , the psinon-antipsinon states $n\psi\psi^*$ ($n = 1, 2$), the two-string states and three-string states in S^{+-} , respectively. In (a), the pink and blue curves overlap significantly and so do the red and black curves in (c).

where $\alpha_{\perp} = -e_0 - \Delta\partial e_0/\partial\Delta + mh$ and $\beta_{\perp} = (2 - \Delta^2)\partial e_0/\partial\Delta + \Delta e_0$. To evaluate the saturation levels, we define the ratio of the momentum-resolved FFMs as

$$v_{\perp}^{(1)}(q) = \tilde{W}_{\perp}(q)/W_{\perp}(q), \quad (7)$$

where $\tilde{W}_{\perp}(q)$ is calculated from the partial summations over the selected excitations.

The calculated momentum-resolved transverse FFM ratios $v_{\perp}^{(1)}(q)$ in the Brillouin zone are displayed in Fig. 1 for three representative magnetizations of $2m = 0.2, 0.5$, and 0.8 . The magnetic polarization breaks time-reversal symmetry, and thus S^{+-} contributes more prominently than S^{-+} to sum rules. We start with plotting S^{-+} contributions, which take into account the ‘‘psinon’’-pair states $n\psi\psi$ ($n = 1, 2$) with n the pair number. These eigenstates possess real rapidities [32,60] and their Bethe quantum numbers are presented in Appendix A.

The S^{+-} channel is more involved: Dominant excitations include the ‘‘psinon-antipsinon’’ pair states denoted as $n\psi\psi^*$ and string states. Combined with S^{-+} , different contributions are plotted and their relative weights are displayed explicitly. The $n\psi\psi^*$ excitations are with real rapidities and their Bethe quantum numbers are given in Appendix A. These states with $n = 1$ and 2 contribute significantly to $S^{+-}(q, \omega)$ at high polarizations, particularly at long wave lengths. But their weights become less important as polarization decreases. This observation is supported by considering the limit of $2m \rightarrow 0$ at $S_T^z = 1$, then $|\mu\rangle$'s in Eq. (2) belong to the subspace of $S_T^z = 0$, whose dimension is $N!/(N/2!)^2$. In this sector, there only exist two states with all real rapidities representing even and odd superpositions of two symmetry breaking Néel states. The dominant weights near the critical line $h_c(\Delta)$ should arise from string states.

The calculation for $S^{+-}(q, \omega)$ is significantly improved by including the string state contributions shown in Fig. 1. The two-string excitations $1\chi^{(2)}R$ ($R = 1\psi\psi^*, 1\psi\psi$) greatly improve the saturation level of the FFM ratios for both intermediate and high polarizations at all momenta. In particular, the $1\chi^{(2)}1\psi\psi^*$ contributions are more dominant than $1\chi^{(2)}1\psi\psi$, typically one order higher. However, at small polarizations, the two-string contributions decrease quickly in particular at long wavelengths, indicating the necessity of including states

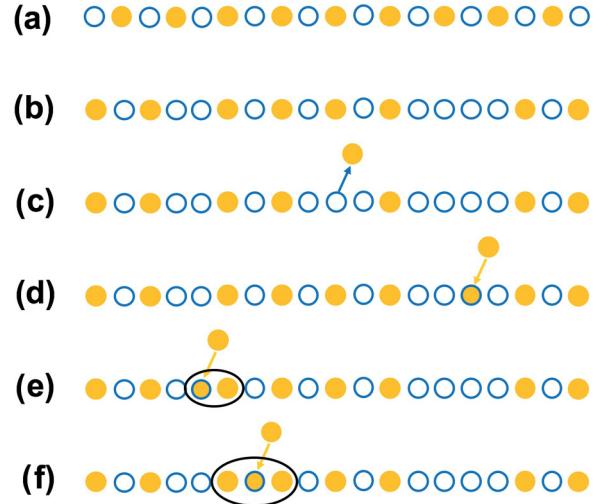


FIG. 2. Schematic plot of a representative spin configuration in the real space within: (a) the Néel ordered ground state at zero field; (b) the incommensurate ground state at a nonzero field $h > h_c$; (c) a state with real particle wave vectors contributing to S^{-+} ; (d) a state with real particle wave vectors contributing to S^{+-} ; (e) a two-string state contributing to S^{-+} ; (f) a three-string state contributing to S^{+-} . The blue hollow circle represents a spin up which is viewed as vacuum, and the yellow solid circle represents a spin down which is viewed as a particle. A particle is removed from (added to) the incommensurate ground state configuration in S^{-+} (S^{+-}), which is represented by an arrow pointing out of (into) the corresponding position in (b).

with even longer strings. Including the three-string excitations $1\chi^{(3)}1\psi\psi^*$ further improves the saturation level of $v_{\perp}^{(1)}(q)$ at small polarizations, while their contributions are minor above the half polarization. The $1\chi^{(3)}1\psi\psi$ excitations are neglected since their contributions are about two orders smaller. After combining all the excitations above, a high saturation level ($>80\%$) is reached for all momenta at the intermediate (e.g., $2m = 0.5$) and high polarizations (e.g., $2m = 0.8$). At small polarizations (e.g., $2m = 0.2$), $v_{\perp}^{(1)}(q)$ is still well saturated for most momenta. Nevertheless, the saturation level decreases when $m \rightarrow 0$ at $q = 0$, and the trend is more prominent for even smaller polarization. There may exist unknown modes with significant weights around zero momentum.

B. String states and spin dynamics

The appearance of string states can be inferred based on an intuitive physical picture. Figure 2(a) shows a pictorial plot of a representative spin configuration in the Néel ordered ground state at zero field. The system becomes incommensurate at $h > h_c$ as shown in Fig. 2(b), but there is still a reminiscence of the Néel ordering when the magnetization is small. The excited states contributing to S^{-+} have one less particle than the ground state. As shown in Fig. 2(c), removing a particle leads to a configuration which still consists of unbound particles. Hence the dominant excitations in S^{-+} are Bethe eigenstates with real rapidities.

On the other hand, the states in S^{+-} have one more particle than the ground state and the situation is more complicated with three possibilities. If the particle is added into the region

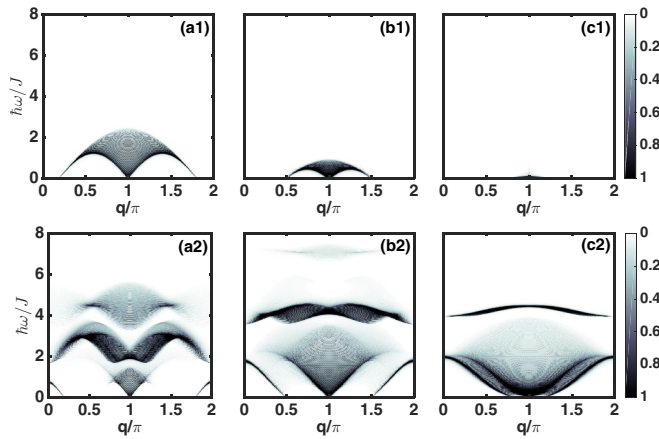


FIG. 3. The intensity plots for the transverse DSFs $S^{++}(q, \omega)$ from (a₁) to (c₁) and $S^{+-}(q, \omega)$ from (a₂) to (c₂) in the q - ω plane all with the same intensity scale. $2m$ equals 0.2 in (a_{1,2}), 0.5 in (b_{1,2}), and 0.8 in (c_{1,2}). The δ function in Eq. (2) is broadened via a Lorentzian function $\frac{1}{\pi} \gamma / [(\omega - E_\mu + E_G)^2 + \gamma^2]$ with $\gamma = 1/400$.

where the Néel ordering is absent, all particles in the resulted excited state remain to be unbounded as shown in Fig. 2(d). The second possibility is to bind the new particle with another existing particle, which gives a two-string state displayed in Fig. 2(e). Figure 2(f) plots the third possibility of a three-string state: The additional particle can be inserted into the middle position of two particles and they form a three-body bounded entity. Based on the above configuration of a diluted Néel ordering state, adding a particle cannot create four particles in a row, hence string states of higher orders occur with much rarer chances, mainly as high order fluctuation effects. Therefore, the S^{+-} DSSF should be dominated by the above three types of excited states. We also expect that the roles played by string states will diminish as increasing the magnetic polarization but are enhanced by increasing the anisotropy. These intuitive considerations are supported by the Bethe ansatz calculations to be discussed below.

C. The spectral weights

The intensity plots of the transverse DSSFs are presented in the q - ω plane in Fig. 3 at representative values of $2m$. The spectra of $S^{++}(q, \omega)$ exhibit the reminiscence of the DCP modes at zero field [58] shown in Figs. 3(a1), 3(b1), and 3(c1) but are significant only in the momentum interval of $2m\pi < q < 2\pi - 2m\pi$. This can be understood intuitively in terms of the 1D Hubbard chain at half filling. Although a weak coupling picture is employed below, charge gap already opens at infinitesimal $U > 0$ and there is no phase transition. The gapless excitations are insensitive to the high energy charge sector, hence, we expect the analysis below should also apply to the case of AFM spin chains. At magnetization m , the Fermi points for two spin components split exhibiting the Fermi wave vectors $k_{f,\downarrow} = \pi(\frac{1}{2} \pm m)$. The minimum momentum for flipping a spin down to up is the difference between $k_{f,\downarrow}$, i.e., $\Delta k_f = 2m\pi$ or equivalently $(1 - m)2\pi$, and the energy cost is zero. At small polarizations, $S^{++}(q, \omega)$ is very coherent near $q = \Delta k_f$, while as q approaches π , it becomes

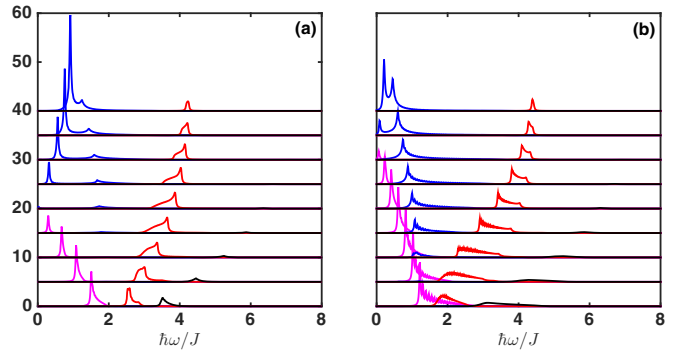


FIG. 4. Spectrum intensity evolution of $S^+(q, \omega) = S^{++}(q, \omega) + S^{+-}(q, \omega)$ vs $\hbar\omega/J$ at (a) $q = \frac{\pi}{2}$, and (b) $q = \frac{3\pi}{4}$. In (a) and (b), lines from bottom to top correspond to $2m$ varying from 0.1 to 0.9 with the step of 0.1. Contributions from psinon excitations in the S^{++} channel are plotted in pink. Psinon-antipsinon, two-string, and three-string states in the S^{+-} channel are plotted in blue, red, and black colors, respectively. The broadening parameter $\gamma = 1/50$.

a continuum. The lower boundary of the continuum touches zero at $q = \pi$ corresponding to flipping a spin down at one Fermi point and adding it to the spin-up Fermi point on the opposite direction. The momentum interval for S^{++} shrinks as increasing polarization and vanishes at the full polarization.

The spectra of $S^{+-}(q, \omega)$ are presented in Figs. 3(a2), 3(b2), and 3(c2). At small polarizations, the spectra resemble the DCP modes and further split into three sectors. Recall the ground state evolution as increasing polarization: At $\Delta > 1$, the ground state exhibits the Néel ordering at $m = 0$ or the commensurate charge-density wave (CDW) of particles. With hole doping, the ground state quantum-mechanically melts and becomes incommensurate. The low energy excitations are thus gapless, however, the intermediate and high energy excitations still sense the gapped Néel state. Applying $S^-(q)$ on $|G\rangle$ corresponds to adding back one particle. A prominent spectra feature at low energy is the coherent Larmor precession mode. At $q = 0$ and the isotropic case, the Larmor precession mode describes the rigid body rotation with the eigenfrequency $\omega = h$ unrenormalized by interaction. With anisotropy and away from $q = 0$, it is renormalized by interaction but remains sharp. The antiferromagnetic coupling causes the downturn of the dispersion touching zero at $q = \pm 2\pi m$ and then disappears. The spectra around $q = \pi$ is incoherent as a reminiscence of the two-spinon continuum in the zero-field DCP mode. The intermediate and high energy spectra arise from the two- and three-string states describing two- and three-particle bound states, respectively. The energy separations among these three sectors are the reminiscence of the spin gap of the Néel state. With increasing polarization, the Larmor mode evolves to the magnon mode. The states containing a pair of bounded magnons contribute to the upper dynamical branch, which are high energy modes since the coupling is antiferromagnetic.

We explicitly display the transverse DSF intensities vs $\hbar\omega/J$ from small to large polarizations at two representative wave vectors $q = \frac{\pi}{2}$ and $\frac{3\pi}{4}$ shown in Fig. 4. The peaks reflect the large-weight region of the spectra in Fig. 3. The low frequency peaks are typically from the two-particle excitations

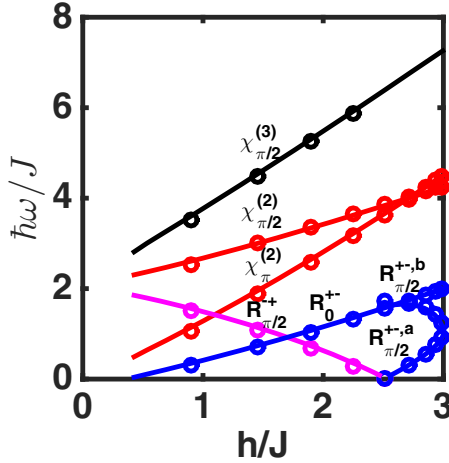


FIG. 5. The evolution of peaks in DSSFs of S^{+-} and S^{-+} at different momenta versus magnetic field h with lines of peaks marked by $\chi_{\pi/2}^{(3)}$, $\chi_{\pi/2}^{(2)}$, $R_{\pi/2}^{+-}$, $\chi_{\pi}^{(2)}$, R_0^{+-} , $R_{\pi/2}^{+-,a}$, and $R_{\pi/2}^{+-,b}$. The pink, blue, red, and black colors correspond to real states in S^{+-} , two-string states in S^{+-} , and three-string states in S^{+-} , respectively. The hollow circles represent the peak positions extracted from DSSF spectral figures similar to Fig. 4. The solid lines are determined by solving the energies of the Bethe eigenstates with the largest weight values around the spectral peaks.

of the $1\psi\psi$ and $1\psi\psi^*$ states. In contrast, the intermediate and high frequency peaks are based on multiparticle string state excitations. For example, the 2-string states $1\chi^{(2)}1\psi\psi$ are four-particle excitations composed of a two-particle bound state and a psinon-psinon pair excitation. Therefore, the string-state-based peaks are typically more smeared than the low frequency peaks.

The evolutions of the spectral peaks at momenta 0 , $\frac{\pi}{2}$, and π as tuning the magnetic field are displayed in Fig. 5. We identify the lines of peaks

$$\chi_{\pi/2}^{(3)}, \chi_{\pi/2}^{(2)}, R_{\pi/2}^{+-}, \chi_{\pi}^{(2)}, R_0^{+-}, R_{\pi/2}^{+-,a}, R_{\pi/2}^{+-,b}, \quad (8)$$

where the subscripts denote the corresponding momenta, and a, b label the two branches of peaks in $R_{\pi/2}^{+-}$. The positions of the hollow circles are determined as follows: We locate the spectral peak frequency position of each channel at the corresponding momenta. Further, the Bethe states with the largest spectral weight and the associated quantum numbers can be identified, and the corresponding eigenenergies are plotted by solid lines in Fig. 5 which indeed pass through the hollow circles.

Here we briefly summarize these states, with details included in Appendix F. For the three-string states $1\chi_{\pi/2}^{(3)}1\psi\psi^*$, which consist of a three-string, one psinon, and one antipinon, the Bethe eigenstate at the peak position of $S^{+-}(q, \omega)$ is characterized with the partition of momenta as

$$k_{\chi^{(3)}} = \pi(1 - m), k_{\psi} = 0, k_{\psi^*} = \pi\left(\frac{1}{2} + m\right), \quad (9)$$

where k denotes the momentum, m is the magnetization per site, and the subscripts in k represents the type of the excitation. For the two-string states $1\chi_{\pi/2}^{(2)}1\psi\psi^*$, the momentum partition is

$$k_{\chi^{(2)}} = \pi(1 + m), k_{\psi} = \pi, k_{\psi^*} = \pi\left(\frac{3}{2} - m\right). \quad (10)$$

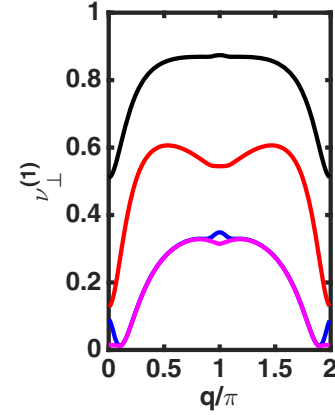


FIG. 6. The momentum-resolved FFM ratios at $2m = 0.1$. The pink, blue, red, and black curves represent cumulative results by including the psinon states $n\psi\psi$ ($n = 1, 2$) in S^{-+} , the psinon-antipinon states $n\psi\psi^*$ ($n = 1, 2$), the two-string states and three-string states in S^{+-} , respectively, as before. The anisotropy $\Delta = 2$, and system size $N = 200$.

Similarly, that of $\chi_{\pi}^{(2)}$ is

$$k_{\chi^{(2)}} = \pi(1 - 2m), k_{\psi} = k_{\psi^*} = \pi\left(\frac{1}{2} + m\right). \quad (11)$$

The spectral peaks from states of real momenta are located at boundaries of the two-particle continuum, which is an analog of the x-ray edge singularity [62,63]. For the following excitations, their momentum partitions are

$$\begin{aligned} R_{\pi/2}^{-+} : k_{\psi_1} &= \pi\left(\frac{1}{2} + m\right), & k_{\psi_2} &= \pi(1 - m), \\ R_0^{+-} : k_{\psi} &= \pi\left(\frac{1}{2} + m\right), & k_{\psi^*} &= \pi\left(\frac{1}{2} - m\right), \\ R_{\pi/2}^{+-,a} : k_{\psi} &= \pi\left(\frac{1}{2} + m\right), & k_{\psi^*} &= \pi(1 - m), \\ R_{\pi/2}^{+-,b} : k_{\psi} &= \pi\left(\frac{3}{2} - m\right), & k_{\psi^*} &= \pi m. \end{aligned} \quad (12)$$

In all of the above cases, to obtain the momentum transfer q in Eq. (2), an additional π shift must be added since S^{+-} and S^{-+} change the ground state magnetization by 1. It is interesting to note that several lines in Fig. 5 exhibit nearly linear relation. The identification of the above Bethe eigenstates is useful for an analytic analysis of the spectral peaks in the thermodynamic limit, which will be left for a more careful future study.

D. More discussions on transverse DSFs

To further investigate the behavior of the transverse DSFs near the critical point, we present the FFM ratio at $2m = 0.1$ in Fig. 6. A high saturation level ($>80\%$) is reached for most momenta, however, near $q = 0$, $\nu_{\perp}^{(1)}(q)$ drops to about 50%. This indicates that there may exist unknown modes with significant weights around zero momentum.

We also investigate the relation of the transverse DSSFs with the anisotropy parameter Δ as shown in Fig. 7. We use the momentum-integrated sum rule [64]

$$R_{a\bar{a}} = \frac{1}{N} \sum_q \int_0^{\infty} \frac{d\omega}{2\pi} S^{a,\bar{a}}(q, \omega) = \frac{1}{4} + \frac{m}{2} c_a, \quad (13)$$

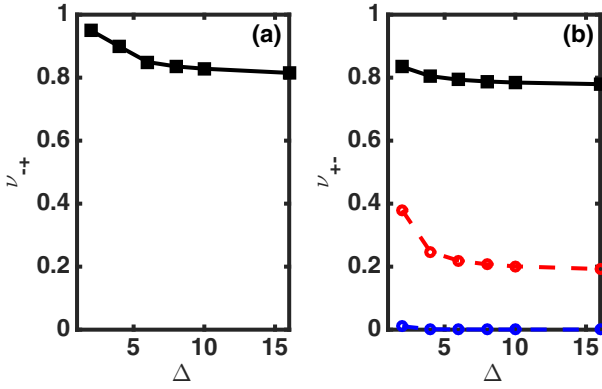


FIG. 7. The Δ dependence of the ratios of momentum integrated intensity (a) ν_{+-} , and (b) ν_{+-} . The parameter values are $N = 200$ and $2m = 0.05$. In (a), the contributions from $1\psi\psi$ and $2\psi\psi$ states are included. In (b), the blue, red, and black curves display the results by cumulatively including the psinon-antipsinon, two-string, and three-string contributions in S^{+-} , respectively.

where $c_a = \pm 1, 0$ for $a = \pm$ and z , respectively. The saturation ratio for the integrated intensity is defined as $\nu_{aa} = \tilde{R}_{aa}/R_{aa}$ with $a = \pm$ and z , where \tilde{R}_{aa} is from the partial summations over the selected excitations.

The small polarization regime is considered for the example of $2m = 0.05$, and the anisotropy parameter Δ takes values of 2, 4, 6, 8, 10, and 16. For S^{-+} , the contributions to ν_{+-} from the $1\psi\psi$ and $2\psi\psi$ states drop to about 80% as increasing Δ , and the absent weights may arise from string states. For S^{+-} , the dominance of three-string states continuously enhances as increasing Δ towards the Ising limit. While the three-string states become increasingly dominant as approaching the critical line, it is known that there are no strings of length longer than two in the zero magnetic field case [65,66]. A more careful investigation of the regime of very small magnetization will be deferred to a future work.

V. THE LONGITUDINAL DYNAMIC SPIN STRUCTURE FACTOR

In this section, we continue to present the longitudinal DSSF, i.e., $S^{zz}(q, \omega)$ of Eq. (1), and also check the saturation level by using sum rules.

A. The momentum-resolved ratios of the longitudinal DSSF

The momentum resolved longitudinal first frequency moment (FFM) sum rule is known as

$$W_{\parallel}(q) = \int_0^{\infty} \frac{d\omega}{2\pi} \omega S^{zz}(q, \omega) = (1 - \cos q)\alpha_{\parallel} \quad [67], \quad (14)$$

where $\alpha_{\parallel} = -e_0 + \Delta\partial e_0/\partial\Delta$. We define the ratio of $\nu_{\parallel}^{(1)}(q) = \tilde{W}_{\parallel}(q)/W_{\parallel}(q)$ in the longitudinal channel, where again $\tilde{W}_{\parallel}(q)$ is calculated from the partial summations over the selected excitations.

The momentum-resolved ratios $\nu_{\parallel}^{(1)}(q)$ at representative polarizations and the intensities of $S^{zz}(q, \omega)$ are plotted in Fig. 8 after taking into account excitations of $1\psi\psi^*$,

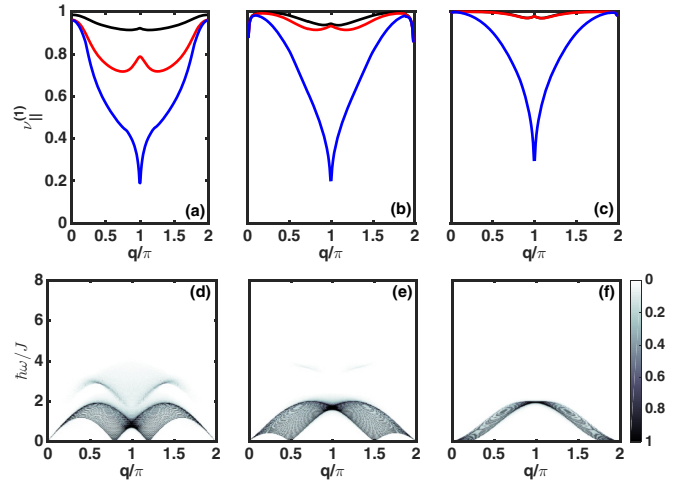


FIG. 8. The momentum-resolved FFM $\nu_{\parallel}^{(1)}(q)$ ratios from (a) to (c), and the intensity plots from (d) to (f) for the longitudinal DSF S^{zz} . $2m$ equals 0.2 in (a) and (d), 0.5 in (b) and (e), and 0.8 in (c) and (f), respectively. In (a), (b), and (c), the blue, red, and black lines are cumulative results by including $1\psi\psi^*$, $2\psi\psi^*$, and $1\chi^{(2)}1\psi\psi$ excitations. The broadening parameter in the intensity plots is $\gamma = 1/400$.

$2\psi\psi^*$, and $1\chi^{(2)}1\psi\psi$ states. Satisfactory saturation levels are obtained.

B. The spectral weights

The calculated spectra weights are plotted in Figs. 8(d), 8(e) and 8(f) for $2m = 0.2, 0.5$, and 0.8 , respectively. This quantity is equivalent to the dynamic density-density correlations of a 1D interacting spinless fermion system through the Jordan-Wigner transformation with the identification of the Fermi wave vector $k_f = \frac{\pi}{2}(1 - 2m)$.

At small polarizations, the contribution of string states dominates the high energy spectra branch. The low energy excitations in the long wavelength regime are very coherent due to the structure of 1D phase space, while those at $2k_f$ are incoherent, both of which can be described by the 1D Luttinger liquid theory [68]. The high energy excitations are the reminiscence of the gapped excitonic excitations in the commensurate Néel background. With increasing polarization, particle filling touches the band bottom where the band curvature is important, and thus the low energy coherent excitations are suppressed and particle-hole continuum becomes more prominent. When the ground state evolves further away towards the full polarization, the low energy excitations are more incoherent, and the spectra from the string state excitations diminish.

VI. DISCUSSION AND CONCLUSION

We discuss the implication of our results for experiments. The quasi-1D $\text{SrCo}_2\text{V}_2\text{O}_8$ AFM chain can be effectively described by the XXZ model with parameters $\Delta = 2$, $J = 3.55\text{meV}$, and the Landé factor $g_z = 6.2$, and the critical value of magnetic field is about $h_c = 4T$ [47,59]. The Brillouin zone of the material is folded into a fourth due to its fourfold screw periodic structure, hence the electronic

spin resonance (ESR) measurements can detect the DSF of $S^{+-} + S^{-+}$ at momenta $0, \frac{\pi}{2}, \pi,$ and $\frac{3\pi}{2}$, in which $\frac{\pi}{2}$ and $\frac{3\pi}{2}$ are equivalent due to the inversion symmetry of the Hamiltonian in Eq. (1). Indeed, the ESR experiment on the material $\text{SrCo}_2\text{V}_2\text{O}_8$ [59] not only confirms the real excitations but also clearly observes the string excitations, in which the experimental results agree well with our theoretical predictions in Fig. 5, demonstrating a rare success of the strong-correlation description for the real material from low to high energy regions [59]. Furthermore, the quantity $1/2(S^{+-} + S^{-+}) + S^{zz}$ can be compared with inelastic neutron scattering experiments for the whole range of (q, ω) .

Besides the spin system, the 1D bosonic system in the hard-core regime is equivalent to the spin- $\frac{1}{2}$ chain, which has been realized in cold atom experiments [69], and quantum dynamics of two-magnon bound states has been measured [9]. Our DSSF calculations and various identified excitations provide helpful guidance to the experimental study of quantum spin dynamics in these systems.

Although the above concrete calculations are based on the integrity of the 1D spin- $\frac{1}{2}$ XXZ model, we believe that the underlying physics at high energies is universal not limited to integrable models. Based on Figs. 2(e) and 2(f), we have explained the physical picture of two and three-string states and the absence of four-string states. Similar physics is also speculated in nonintegrable models, such as in the two-dimensional AFM XXZ model. Under similar physical parameter setups, we would expect it is possible to observe contributions from two, three, four, and up to five-magnon clustering states, since in a two-dimensional geometry the coordination number is 4. Certainly for the 2D case, the method of Bethe ansatz will not be possible, and the theory study will be deferred to a future publication.

In summary, the zero temperature spin dynamics is studied for the spin- $\frac{1}{2}$ AFM XXZ model in the longitudinal magnetic field. We find that different dynamic branches are energetically separated, which originate from various classes of excitations including psinon-psinon and psinon-antipsinon pairs at low energy and string excitations at intermediate and high energies. In particular, for $S^{+-}(q, \omega)$ at small magnetizations, states with real rapidities contribute negligibly small to the sum rule, and the three-string states become more and more dominant as approaching the critical line or increasing anisotropy. These high-frequency spin dynamic features cannot be captured within the low energy effective theory of the Luttinger liquid. Our calculations provide important guidance for analyzing the 1D spin dynamics experiments in both condensed matter and ultracold atom systems.

ACKNOWLEDGMENTS

We thank Matthew Foster useful discussions. W.Y., J.W., S.X., and C.W. are supported by the AFOSR FA9550-14-1-0168. C.W. is also supported by the UC Multicampus Research Programs and Initiatives under the Grant No. MRP-19-601445.

APPENDIX A: BETHE ANSATZ IN THE AXIAL REGIME

In this section, we present the Bethe ansatz equations (BAE) and the Bethe quantum number (BQN) structure. We

focus on the antiferromagnetic XXZ spin chain [Eq. (1) in the main text] in the axial regime with $\Delta = \cosh \eta > 1$.

In the method of the algebraic Bethe ansatz [18], the monodromy matrix is a 2×2 matrix. Its matrix entries $A(\lambda), B(\lambda), C(\lambda), D(\lambda)$ are operators acting in the many-body Hilbert space of the spin chain. By virtue of the Yang-Baxter equation, all the transfer matrices $T(\lambda) = A(\lambda) + D(\lambda)$ with different spectral parameter λ 's commute, hence they can be simultaneously diagonalized. The XXZ Hamiltonian can be expressed in terms of these transfer matrices, and thus it shares common eigenstates with all the transfer matrices.

A Bethe eigenstate with M down spins can be expressed as the result of successively applying the magnon creation operators $B(\lambda_j)$ ($1 \leq j \leq M$) onto the reference state $|F\rangle = \otimes_{j=1}^N |\uparrow\rangle_j$, as $\prod_{j=1}^M B(\lambda_j)|F\rangle$. The rapidities $\{\lambda_j\}_{1 \leq j \leq M}$ satisfy the Bethe ansatz equations,

$$N\theta_1(\lambda_j) = 2\pi I_j + \sum_{k=1}^M \theta_2(\lambda_j - \lambda_k), \quad (\text{A1})$$

where

$$\theta_n(\lambda) = 2 \arctan \left(\frac{\tan(\lambda)}{\tanh(n\eta/2)} \right) + 2\pi \left\lfloor \frac{\text{Re}(\lambda)}{\pi} + \frac{1}{2} \right\rfloor. \quad (\text{A2})$$

The symbol $\lfloor x \rfloor$ represents the floor function, which yields the largest integer less than or equal to x .

The rapidities can be either real or complex in general. If all λ_j 's are real, then the corresponding state is called a real Bethe eigenstate. If there exist complex valued λ_j 's, then the state is called a string state [20], whose name comes from the pattern of λ_j 's in the complex plane in the thermodynamic limit. We will give a brief description in Appendix B.

For a chain with an even number of sites, the ascending array of Bethe quantum numbers $\{I_j\}_{1 \leq j \leq M}$ takes integer values when M is odd and half-integer values when M is even. The total momentum of this state is

$$P = \pi M - \frac{2\pi}{N} \sum_{j=1}^M I_j, \quad (\text{A3})$$

and the energy is

$$E = \sum_{j=1}^M \frac{\sinh^2(\eta)}{\cosh \eta - \cos(2\lambda_j)}. \quad (\text{A4})$$

In the subspace with a fixed value of S_T^z , there exist $M = \frac{N}{2} - S_T^z$ down spins. In this sector, the BQN of the lowest energy state are given by

$$I_j = -\frac{M+1}{2} + j, \quad 1 \leq j \leq M. \quad (\text{A5})$$

As for the excited states, the BQN can be grouped into certain patterns by examining how they can be obtained through modifying those in the ground state given in Eq. (A5). We consider two different classes of excited states with purely real rapidities. Eigenstates with an n pair of psinons are denoted $n\psi\psi$ [28], and their Bethe quantum numbers $\{I_j\}_{1 \leq j \leq M}$ satisfy

$$-\frac{M-1}{2} - n \leq I_j \leq \frac{M-1}{2} + n, \quad (\text{A6})$$

where either $I_1 = -\frac{M-1}{2} - n$ or $I_M = \frac{M-1}{2} + n$ to avoid overcounting. Another class of solutions is called n pair of psinon-antipsinon states denoted $n\psi\psi^*$. Among their M Bethe quantum numbers I_j 's, $M-n$ of them lying within the range $[-\frac{M-1}{2}, \frac{M-1}{2}]$, and the remaining n ones lying outside [28].

APPENDIX B: THE BETHE-GAUDIN-TAKAHASHI EQUATIONS FOR STRING STATES

The rapidities of the BAE can take complex values, and the corresponding solutions are called string states [20]. The string ansatz assumes that the complex rapidities form the string pattern described below.

For a single n string of complex rapidities,

$$\lambda_j^n = \lambda^{(n)} + i(n+1-2j)\frac{\eta}{2}, \quad 1 \leq j \leq n, \quad (\text{B1})$$

where $\lambda^{(n)}$ and η are real numbers, and j is the rapidity index inside the string. For a finite system the distribution of rapidities does not exactly follow Eq. (B1). The deviations become exponentially suppressed as enlarging system size, and the string ansatz is asymptotically exact in the thermodynamic limit. Then a general Bethe eigenstate with M rapidities is a collection of M_n n strings, where $\sum_n nM_n = M$. A real Bethe eigenstate can be also viewed as a collection of M one strings in this language.

The BAE Eq. (A1) becomes singular in thermodynamic limit for a string state with the rapidity pattern of Eq. (B1). Their regularized version is called the Bethe-Gaudin-Takahashi (BGT) equations [20], which only contain the common real part $\lambda^{(n)}$

$$N\theta_n(\lambda_\alpha) = 2\pi I_\alpha^{(n)} + \sum_{(m,\beta) \neq (n,\alpha)} \Theta_{nm}(\lambda_\alpha^{(n)} - \lambda_\beta^{(m)}), \quad (\text{B2})$$

with $1 \leq \alpha \leq M_n$, $1 \leq \beta \leq M_m$, where

$$\Theta_{nm} = (1 - \delta_{nm})\theta_{|n-m|} + 2\theta_{|n-m|+2} + \dots + 2\theta_{n+m-2} + \theta_{n+m}, \quad (\text{B3})$$

and θ_n is defined in Eq. (A2). The momentum of such a state is

$$P = \pi \sum_n M_n - \frac{2\pi}{N} \sum_{n\alpha} I_\alpha^{(n)} \quad (\text{B4})$$

and the energy is

$$E = \sum_{n\alpha} \frac{\sinh(\eta) \sinh(n\eta)}{\cosh(n\eta) - \cos(2\lambda_\alpha^{(n)})}. \quad (\text{B5})$$

The general rules for determining BQN for distinct eigenstates are rather complicated [35]. Since only Bethe eigenstates with up to only two types of strings are considered in this article, we only present the rules for these special cases below [35].

Consider a string state with M_m m strings and M_n n strings, where $M = mM_m + nM_n$. Without loss of generality, we assume $m < n$. The BQN for the m strings are within the sets of

$$A_i^{(m)} = \left\{ -\frac{W_m-1}{2} + i \leq I_j^m \leq \frac{W_m-1}{2} + i, 1 \leq j \leq M_m \right\}, \quad (\text{B6})$$

where

$$W_m = N - 2mM_n - (2m-1)M_m, \quad (\text{B7})$$

and $0 \leq i \leq 2m-1$. For the n strings, the BQN are within the sets of

$$A_i^{(n)} = \left\{ -\frac{W_n-1}{2} + i \leq I_j^n \leq \frac{W_n-1}{2} + i, 1 \leq j \leq M_n \right\}, \quad (\text{B8})$$

where

$$W_n = N - 2mM_m - (2n-1)M_n, \quad (\text{B9})$$

and $0 \leq i \leq 2n-1$. Not all these BQN yield distinct Bethe eigenstates. To remove equivalent sets of BQN giving the same eigenstates, we need to exclude those simultaneously satisfying the following two conditions

$$\begin{aligned} I_1^{(m)} &\leq -\frac{W_m-1}{2} + 2m-1, \\ I_{M_n}^{(n)} &\geq \frac{W_n-1}{2} + 2n - (2m-1). \end{aligned} \quad (\text{B10})$$

In the following, the presence of the rules of Bethe quantum numbers for two-string and three-string states are combined together to reduce the content. We list the rules for the BQN of the string states calculated in the main text. In the following formulas, $n = 2$ or 3 . The rule for $1\chi^{(n)}1\psi\psi^*$ state is

$$\begin{aligned} -\frac{N-2M}{2} &\leq I^{(n)} \leq \frac{N-2M}{2} + 2n-1, \\ -\frac{M-n+1}{2} + i &\leq I_j^{(1)} \leq \frac{M-n+1}{2} + i, \quad 1 \leq j \leq M-n, \end{aligned} \quad (\text{B11})$$

in which i is an integer. The DSF intensity distribution must be symmetric with respect to the momentum π since the system possesses inversion symmetry. It is possible for states with $i = 0$ to be transformed to those with $i \neq 0$ under inversion, which must also be included.

For the excitations of the type of $1\chi^{(n)}1\psi\psi^{(*)}$, the rule for the $I^{(n)}$ part is the same, while that for real rapidities is

$$\begin{aligned} -\frac{M-n-1}{2} + i &\leq I_{j_l}^{(1)} \leq \frac{M-n-1}{2} + i, \\ 1 &\leq l \leq M-n-1, \\ -\frac{N-M+n-3}{2} &\leq I_{j_{M-n}}^{(1)} \leq -\frac{M-n-1}{2} - 1 + i, \text{ or} \\ \frac{M-n-1}{2} + 1 + i &\leq I_{j_{M-n}}^{(1)} \leq \frac{N-M+n-3}{2} + 1, \end{aligned} \quad (\text{B12})$$

where $I_j^{(1)}$'s should be arranged in an ascending array, and $-(2n-1) \leq i \leq 2n-1$ again for the purpose of symmetrization. The BQN need to be excluded if they simultaneously satisfy the following two conditions $I^{(n)} \geq \frac{N-2M}{2} + 2n-2$ and $I_1^{(1)} \leq -\frac{N-M+n-3}{2} + 1$ to avoid overcounting as mentioned above.

APPENDIX C: THE DETERMINANT FORMULAE

To carry out the DSF calculation, the normalized Bethe state and the matrix element of spin operators are needed. The normalized state of $\Pi_{j=1}^M B(\lambda_j)|F\rangle$ is denoted as $|\{\lambda_j\}_{1 \leq j \leq M}\rangle$ below. The matrix entries $\langle\{\mu_k\}_{1 \leq k \leq M+1}|S_q^a|\{\lambda_j\}_{1 \leq j \leq M}\rangle$ can be formulated into determinant forms [70], which greatly facilitates both analytical and numerical calculations.

1. Real states in the axial regime

We first present the determinant formulas for the real Bethe state. Since $|\langle\{\mu_k\}_{1 \leq k \leq M+1}|S_q^-|\{\lambda_j\}_{1 \leq j \leq M}\rangle|^2 = |\langle\{\lambda_j\}_{1 \leq j \leq M}|S_q^+|\{\mu_k\}_{1 \leq k \leq M+1}\rangle|^2$, we only present the matrix element for S_q^- and S_q^z .

The transverse matrix element can be expressed as

$$\begin{aligned} |\langle\{\mu\}|S_q^-|\{\lambda\}\rangle|^2 &= N \delta_{P(\{\lambda\})-P(\{\mu\}),q} |\sin i\eta| \frac{\prod_{k=1}^{M+1} |\sin(\mu_k - i\eta/2)|^2}{\prod_{j=1}^M |\sin(\lambda_j - i\eta/2)|^2} \\ &\times \frac{1}{\prod_{k \neq k'} |\sin(\mu_k - \mu_{k'} + i\eta)| \prod_{j \neq j'} |\sin(\lambda_j - \lambda_{j'} + i\eta)|} \frac{|\det H^-|^2}{|\det \Phi(\{\mu\}) \det \Phi(\{\lambda\})|}. \end{aligned} \quad (C1)$$

in which H^- is an $(M+1) \times (M+1)$ matrix. For $1 \leq k \leq M+1$, $1 \leq j \leq M$,

$$H_{kj}^- = \frac{1}{\sin(\mu_k - \lambda_j)} \left[\prod_{l=1(l \neq k)}^{M+1} \sin(\mu_l - \lambda_j + i\eta) - \left(\frac{\sin(\lambda_j - i\eta/2)}{\sin(\lambda_j + i\eta/2)} \right)^N \prod_{l=1(l \neq k)}^{M+1} \sin(\mu_l - \lambda_j - i\eta) \right]; \quad (C2)$$

and for $1 \leq k \leq M+1$,

$$H_{k,M+1}^- = \frac{1}{\sin(\mu_k + i\eta/2) \sin(\mu_k - i\eta/2)}. \quad (C3)$$

For the longitudinal matrix element, the expression for $\langle\{\mu_k\}_{1 \leq k \leq M}|S_q^z|\{\lambda_j\}_{1 \leq j \leq M}\rangle$ is

$$\begin{aligned} |\langle\{\mu\}|S_q^z|\{\lambda\}\rangle|^2 &= \frac{N}{4} \delta_{P(\{\lambda\})-P(\{\mu\}),q} \prod_{k=1}^M \left| \frac{\sin(\mu_k - i\eta/2)}{\sin(\lambda_j - i\eta/2)} \right|^2 \\ &\times \frac{1}{\prod_{k \neq k'} |\sin(\mu_k - \mu_{k'} + i\eta)| \prod_{j \neq j'} |\sin(\lambda_j - \lambda_{j'} + i\eta)|} \frac{|\det(H - 2P)|^2}{|\det \Phi(\{\mu\}) \det \Phi(\{\lambda\})|}, \end{aligned} \quad (C4)$$

in which the $M \times M$ matrices H and P are given by

$$H_{kj} = \frac{1}{\sin(\mu_k - \lambda_j)} \left[\prod_{l=1(l \neq k)}^M \sin(\mu_l - \lambda_j + i\eta) - \left(\frac{\sin(\lambda_j - i\eta/2)}{\sin(\lambda_j + i\eta/2)} \right)^N \prod_{l=1(l \neq k)}^M \sin(\mu_l - \lambda_j - i\eta) \right], \quad (C5)$$

and

$$P_{kj} = \frac{\prod_{l=1}^M \sin(\lambda_l - \lambda_j - i\eta)}{\sin(\mu_k + i\eta/2) \sin(\mu_k - i\eta/2)}, \quad \text{for } 1 \leq k \leq M, \quad 1 \leq j \leq M. \quad (C6)$$

The off-diagonal matrix element Φ_{jk} at $(j \neq k)$ is

$$\Phi_{jk} = \frac{\sin(2i\eta)}{\sin(\lambda_j - \lambda_k - i\eta) \sin(\lambda_j - \lambda_k + i\eta)}, \quad (C7)$$

and the diagonal matrix element Φ_{jj} is

$$\Phi_{jj} = N \frac{\sin(i\eta)}{\sin(\lambda_j - i\eta/2) \sin(\lambda_j + i\eta/2)} - \sum_{l=1, l \neq j}^M \frac{\sin(2i\eta)}{\sin(\lambda_j - \lambda_l - i\eta) \sin(\lambda_j - \lambda_l + i\eta)}. \quad (C8)$$

2. The reduced determinant formula for string states

In calculating the DSFs, if we directly plug in the rapidities of the string state solutions into Eqs. (C7) and (C8), the matrix Φ becomes singular. The L'Hospital's rule must be applied to remove the singularities [35]. The reduced matrix $\Phi^{(r)}$ is defined

by [35]

$$\begin{aligned} \Phi_{n\alpha, n\alpha}^{(r)} &= N \sum_{j=1}^n \left[\frac{\sin(i\eta)}{\sin(\lambda_j^{(n\alpha)} - i\eta/2) \sin(\lambda_j^{(n\alpha)} + i\eta/2)} - \sum_{k=1(k \neq n\alpha, j, j\pm 1)}^M \frac{\sin(2i\eta)}{\sin(\lambda_j^{(n\alpha)} - \lambda_k - i\eta) \sin(\lambda_j^{(n\alpha)} - \lambda_k + i\eta)} \right. \\ &\quad \left. + \sum_{l=1(l \neq j, j\pm 1)}^n \frac{\sin(2i\eta)}{\sin(\lambda_j^{(n\alpha)} - \lambda_l^{(n\alpha)} - i\eta) \sin(\lambda_j^{(n\alpha)} - \lambda_l^{(n\alpha)} + i\eta)} \right], \\ \Phi_{n\alpha, m\beta}^{(r)} &= \sum_{j=1}^n \sum_{k=1}^m \frac{\sin(2i\eta)}{\sin(\lambda_j^{(n\alpha)} - \lambda_k^{(m\beta)} - i\eta) \sin(\lambda_j^{(n\alpha)} - \lambda_k^{(m\beta)} + i\eta)}, \quad n\alpha \neq m\beta, \end{aligned} \quad (C9)$$

in which $\lambda_j^{(n\alpha)} = \lambda^{(n\alpha)} + i(n+1-2j)\eta/2$, where $\lambda^{(n\alpha)}$ is the common real part of the α 'th length- n string.

The formula for $|\langle \{\mu\} | S_q^- | \{\lambda\} \rangle|^2$, where $|\{\mu\}\rangle$ is a string state, $|\{\lambda\}\rangle$ a real Bethe eigenstate, is given by

$$\begin{aligned} |\langle \{\mu\} | S_q^- | \{\lambda\} \rangle|^2 &= N \delta_{P(\{\lambda\})-P(\{\mu\}), q} \frac{|\sin(i\eta)|}{\prod_n (|\sin^{n-1}(2i\eta)|)^{M_n}} \frac{\prod_{k=1}^{M+1} |\sin(\mu_k + i\eta/2)|}{\prod_{j=1}^M |\sin(\lambda_j + i\eta/2)|} \frac{1}{\prod_{j \neq j'} |\sin(\lambda_j - \lambda_{j'} + i\eta)|} \\ &\quad \times \frac{1}{\prod_{m\beta l \neq n\alpha l', l' \pm 1} |\sin(\mu_l^{(n\alpha)} - \mu_{l'}^{(m\beta)} + i\eta)|} \frac{|\det H^-|^2}{|\det \Phi(\{\lambda\})| \cdot |\det \Phi^r(\{\mu\})|}. \end{aligned} \quad (C10)$$

The expression for $|\langle \{\mu\} | S_q^z | \{\lambda\} \rangle|^2$ can be obtained similarly, as

$$\begin{aligned} |\langle \{\mu\} | S_q^z | \{\lambda\} \rangle|^2 &= \frac{N}{4} \delta_{P(\{\lambda\})-P(\{\mu\}), q} \frac{1}{\prod_n (|\sin^{n-1}(2i\eta)|)^{M_n}} \prod_{j=1}^M \left| \frac{\sin(\mu_j + i\eta/2)}{\sin(\lambda_j + i\eta/2)} \right|^2 \frac{1}{\prod_{j \neq j'} |\sin(\lambda_j - \lambda_{j'} + i\eta)|} \\ &\quad \times \frac{1}{\prod_{m\beta l \neq n\alpha l', l' \pm 1} |\sin(\mu_l^{(n\alpha)} - \mu_{l'}^{(m\beta)} + i\eta)|} \frac{|\det(H - 2P)|^2}{|\det \Phi(\{\lambda\})| \cdot |\det \Phi^r(\{\mu\})|}. \end{aligned} \quad (C11)$$

APPENDIX D: DEVIATION OF STRING STATES

The string ansatz is known to be not exact even in the thermodynamic limit. The solutions of rapidities may deviate from the pattern assumed by string ansatz. Such deviations must be taken into account when they are large [61]. In this section, we give the formulas for an exact treatment of string deviations for $1\chi^{(2)}R$ and $1\chi^{(3)}R$ excitations.

The branch cut of logarithmic function is taken as the negative real axis which is identified with $\mathbb{R}^- + i0$. From this the branch cut of arctan function is accordingly determined via the definition

$$\arctan(z) = \frac{1}{2i} (\ln(1+iz) - \ln(1-iz)). \quad (D1)$$

For a $1\chi^{(2)}R$ type excitation, let the two complex rapidities be $\lambda_{\pm}^{(2)} = \lambda^{(2)} \pm i(\eta/2 + \delta)$, where δ represents the deviation from the pattern of string ansatz, and the remaining $M-2$ real rapidities be $\{\lambda_k\}_{1 \leq k \leq M-2}$. Let the corresponding BQN be J_{\pm} and $\{J_k\}_{1 \leq k \leq M-2}$. Then the two BAE for the complex rapidities are

$$N\theta_1(\lambda_a^{(2)}) = 2\pi J_a + \theta_2(\lambda_a^{(2)} - \lambda_{-a}^{(2)}) + \sum_{k=1}^{M-2} \theta_2(\lambda_a^{(2)} - \lambda_k), \quad (D2)$$

where $a = \pm$. In the following, we assume that $\lambda^{(2)} \neq 0$, $\delta \neq 0$, and $\lambda^{(2)} - \lambda_j \neq 0$, $1 \leq j \leq M-2$.

From the choice of branch cut for arctan function, the real part of the difference between the equations of $a = +$ and $a = -$ in Eq. (D2) gives

$$J_- - J_+ = \Theta(\delta), \quad (D3)$$

in which $\Theta(x) = 1$ when $x \geq 0$ and $\Theta(x) = 0$ when $x < 0$. Taking the sum of the equations for $a = +$ and $a = -$ in Eq. (D2), setting $\delta = 0$, and comparing with the reduced BGT equation, we obtain

$$J_- + J_+ = I^{(2)} + N \left[\frac{\lambda^{(2)}}{\pi} + \frac{1}{2} \right] + \frac{N}{2} (-)^{\lfloor \frac{\lambda^{(2)}}{\pi/2} \rfloor}. \quad (D4)$$

The sign of δ can be determined from Eq. (D4) by noticing that J_{\pm} are integers (half integers) when M is odd (even), i.e.,

$$\Theta(\delta) = \text{mod} \left(I^{(2)} - M + 1 + \frac{N}{2}, 2 \right). \quad (D5)$$

Combining Eqs. (D4) and (D5) together, the BQN J_{\pm} can be determined from the reduced one $I^{(2)}$ in BGT equations. For the BQN of real rapidities, it can be shown that $J_k = I_k$, $1 \leq k \leq M-2$. To solve the exact values of rapidities, Eq. (D2) is replaced with the following two real equations. The first one is the sum of the two equations in Eq. (D2) but not setting $\delta = 0$. The second one is obtained by taking the imaginary part of the $a = +$ equations in Eq. (D2), as

$$\begin{aligned} &\left| \frac{\tan(\lambda_+^{(2)} - \lambda_-^{(2)}) - i \tanh \eta}{\tan(\lambda_+^{(2)} - \lambda_-^{(2)}) + i \tanh \eta} \right| \\ &= \left| \frac{\tan(\lambda_+^{(2)}) - i \tanh \eta/2}{\tan(\lambda_+^{(2)}) + i \tanh \eta/2} \right|^N \cdot \prod_k \left| \frac{\tan(\lambda_+^{(2)} - \lambda_k) + i \tanh \eta}{\tan(\lambda_+^{(2)} - \lambda_k) - i \tanh \eta} \right|. \end{aligned} \quad (D6)$$

Combining these two equations with the BAE for real rapidities, the exact solutions can be solved. The first order deviation

of δ can be obtained from Eq. (D6). Up to first order of δ , the left hand side (LHS) of Eq. (D6) is $|\delta|/(\sinh(\eta) \cosh(\eta))$.

For the case of $1\chi^{(3)}R$ excitation, the logic is similar. Let the three complex rapidities be $\lambda_a^{(3)}$ with $a = \pm, 0$ and the real rapidities be $\{\lambda_k\}_{1 \leq k \leq M-3}$. Let the corresponding Bethe quantum numbers be J_a ($a = \pm, 0$) and $\{J_k\}_{1 \leq k \leq M-3}$. To parametrize the string deviations, the complex rapidities are written as $\lambda_0^{(3)} = \lambda^{(3)}$ and $\lambda_{\pm}^{(3)} = \lambda^{(3)} + \epsilon \pm i(\eta + \delta)$. The BAE for the three complex rapidities are

$$N\theta_1(\lambda_a^{(3)}) = 2\pi J_a + \sum_{b \neq a} \theta_2(\lambda_a^{(3)} - \lambda_b^{(3)}) \sum_{k=1}^{M-3} \theta_2(\lambda_a^{(3)} - \lambda_k), \quad (\text{D7})$$

where $a, b = \pm, 0$. We assume that $\lambda^{(3)} \neq 0$, $\epsilon \neq 0$, $\delta \neq 0$, and $\lambda^{(3)} - \lambda_j \neq 0$, $1 \leq j \leq M-3$.

The real part of the difference between the equations for $a = +$ and $a = -$ in Eq. (D7) gives

$$J_- - J_+ = 1. \quad (\text{D8})$$

Taking the sum of the three equations in Eq. (D7), setting $\epsilon = \delta = 0$, and comparing with the reduced BGT equation, we obtain

$$J_+ + J_0 + J_- = I^{(3)} + N \left(2 \left[\frac{\lambda^{(3)}}{\pi} + \frac{1}{2} \right] + (-)^{\lfloor \frac{\lambda^{(3)}}{\pi/2} \rfloor} \right) - \sum_k \left(\left[\frac{\lambda^{(3)} - \lambda_k}{\pi} + \frac{1}{2} \right] + \frac{1}{2} (-)^{\lfloor \frac{\lambda^{(3)} - \lambda_k}{\pi/2} \rfloor} \right). \quad (\text{D9})$$

To determine J_{\pm} and J_0 , the sum of the equations for $a = \pm$ in Eq. (D7) is taken, yielding

$$\begin{aligned} 2\pi(J_+ + J_-) + \theta_2(\lambda_+^{(3)} - \lambda_0^{(3)}) + \theta_2(\lambda_-^{(3)} - \lambda_0^{(3)}) \\ = N(\theta_1(\lambda_+^{(3)}) + \theta_1(\lambda_-^{(3)})) \\ - \sum_k (\theta_2(\lambda_+^{(3)} - \lambda_k) + \theta_2(\lambda_-^{(3)} - \lambda_k)). \end{aligned} \quad (\text{D10})$$

Define A to be the right hand side of Eq. (D10). Since $\theta_2(\lambda_+^{(3)} - \lambda_0) + \theta_2(\lambda_-^{(3)} - \lambda_0) \in (-2\pi, 2\pi)$, $J_+ + J_-$ is the even (odd) integer number within $(A/2\pi - 1, A/2\pi + 1)$ when M is even (odd). Hence

$$\begin{aligned} J_+ + J_- = (1 + (-)^M) \left[\frac{1}{2} \left(\frac{A}{2\pi} + 1 \right) \right] + (1 - (-)^M) \\ \times \left(\left[\frac{1}{2} \left(\frac{A}{2\pi} + 1 \right) + \frac{1}{2} \right] - \frac{1}{2} \right). \end{aligned} \quad (\text{D11})$$

From Eqs. (D8), (D9), and (D11), the values of J_{\pm} and J_0 can be determined from the reduced BQN $I^{(3)}$ in the BGT equation. The BQN for real rapidities can be proved to be of the following expression in a similar manner,

$$J_k = I_k - \left[\frac{\lambda_k - \lambda^{(3)}}{\pi} + \frac{1}{2} \right] - \frac{1}{2} (-)^{\lfloor \frac{\lambda_k - \lambda^{(3)}}{\pi/2} \rfloor}, \quad (\text{D12})$$

where $1 \leq k \leq M-3$.

For solving rapidities, Eq. (D7) is replaced with the following three real equations. The first one is the sum of the equations for $a = \pm, a = 0$ in Eq. (D7) without setting ϵ and δ to be zero. The second one is Eq. (D10). The third one is

by taking the imaginary part of the difference between the equations for $a = +$ and $a = -$ in Eq. (D10), which is

$$\begin{aligned} \left| \frac{\tan(\lambda_+^{(3)} - \lambda_0^{(3)}) - i \tanh \eta}{\tan(\lambda_+^{(3)} - \lambda_0^{(3)}) + i \tanh \eta} \right| \\ = \left| \frac{\tan(\lambda_+^{(3)} - \lambda_-^{(3)}) + i \tanh \eta}{\tan(\lambda_+^{(3)} - \lambda_-^{(3)}) - i \tanh \eta} \right| \cdot \left| \frac{\tan(\lambda_+^{(3)}) - i \tanh \eta/2}{\tan(\lambda_+^{(3)}) + i \tanh \eta/2} \right|^{2N} \\ \cdot \prod_k \left| \frac{\tan(\lambda_+^{(2)} - \lambda_k) + i \tanh \eta}{\tan(\lambda_+^{(2)} - \lambda_k) - i \tanh \eta} \right|. \end{aligned} \quad (\text{D13})$$

Let $\epsilon = r \sin \theta$, $\delta = r \cos \theta$. For first order deviation, we remark that up to first order in ϵ and δ , the LHS of Eq. (D13) is $r/(2 \sinh \eta \cosh \eta)$, and θ can be determined from Eq. (D10) as

$$\theta = -\phi + \pi \operatorname{sgn} \phi, \quad (\text{D14})$$

in which ϕ is defined to be $\frac{1}{2}A - \pi J_0$. The values of r and θ can be used as the initial inputs in an iterative solution of ϵ and δ .

APPENDIX E: SUM RULES

The momentum-resolved first frequency sum rules are presented below. The transverse first frequency moment (FFM) sum rule is $W_{\perp}(q) = \int_0^{\infty} \frac{d\omega}{2\pi} \omega [S^{+-}(q, \omega) + S^{-+}(q, \omega)] = \alpha_{\perp} + \beta_{\perp} \cos q$, where $\alpha_{\perp} = -e_0 - \Delta \partial e_0 / \partial \Delta + mh$ and $\beta_{\perp} = (2 - \Delta^2) \partial e_0 / \partial \Delta + \Delta e_0$. Its longitudinal version is also known as $W_{\parallel}(q) = \int_0^{\infty} \frac{d\omega}{2\pi} \omega S^{zz}(q, \omega) = (1 - \cos q) \alpha_{\parallel}$ [67], where $\alpha_2 = -e_0 + \Delta \partial e_0 / \partial \Delta$.

Here we summarize the derivation of the first frequency moment sum rule in Eq. (6) following Ref. [67]. The first frequency moment is defined as

$$\omega_{a\bar{a}}(q) = \int_{-\infty}^{\infty} \frac{d\omega}{2\pi} \omega S^{a\bar{a}}(q, \omega). \quad (\text{E1})$$

The expressions of $\omega_{+-} + \omega_{-+}$ and ω_{zz} are derived as a function of Δ and h for the XXZ Hamiltonian [Eq. (1) in the main text].

By inserting a complete set of eigenstates and performing the integration with respect to t and ω , ω_{ii} ($i = x, y, z$) can be transformed as

$$\begin{aligned} \omega_{ii} = \frac{1}{N} \sum_{j, j'} e^{-iq(j-j')} \int_{-\infty}^{\infty} \frac{d\omega}{2\pi} \int_{-\infty}^{\infty} dt \omega e^{i\omega t} \\ \times \sum_{\mu} e^{i(E_G - E_{\mu})t} \langle G | S_j^i | \mu \rangle \langle \mu | S_{j'}^i | G \rangle \\ = -\frac{1}{N} \sum_{j, j'} e^{-iq(j-j')} \langle G | [H, S_j^i] S_{j'}^i | G \rangle. \end{aligned}$$

Similarly

$$\omega_{ii} = \frac{1}{N} \sum_{j, j'} e^{-iq(j-j')} \langle G | S_j^i [H, S_{j'}^i] | G \rangle. \quad (\text{E2})$$

Since the system is invariant under inversion transformation defined as $P \tilde{S}_j P^{-1} = \tilde{S}_{-j}$, i.e.,

$$P |G\rangle = |G\rangle, \quad P H P^{-1} = H, \quad (\text{E3})$$

Eq. (E2) becomes

$$\omega_{ii} = \frac{1}{N} \sum_{j, j'} e^{-iq(j-j')} \langle G | S_{j'}^i [H, S_j^i] | G \rangle, \quad (\text{E4})$$

where in obtaining the last line the change of summation indices $-j \rightarrow j'$ and $-j' \rightarrow j$ is performed. Combining these results together, we obtain

$$\omega_{ii} = -\frac{1}{2N} \sum_{j,j'} e^{-iq(j-j')} \langle G | [[H, S_j^i], S_{j'}^i] | G \rangle. \quad (\text{E5})$$

The commutation relations for $i = x, y, z$ can be carried out explicitly, and the results for ω_{ii} are

$$\begin{aligned} \omega_{xx(yy)} &= -\frac{1}{N} \sum_j \left[(1 - \Delta \cos q) \langle G | S_j^{y(x)} S_{j+1}^{y(x)} | G \rangle \right. \\ &\quad \left. + (\Delta - \cos q) \langle G | S_j^z S_{j+1}^z | G \rangle - \frac{h}{2} S_j^z \right], \\ \omega_{zz} &= -\frac{1}{N} (1 - \cos q) \sum_j \langle G | (S_j^x S_{j+1}^x + S_j^y S_{j+1}^y) | G \rangle. \end{aligned} \quad (\text{E6})$$

In the main text $S^{+-}(q, \omega)$ and $S^{-+}(q, \omega)$ are calculated, and their first frequency moment sum rule can be derived from ω_{xx} and ω_{yy} through

$$\omega_{+-} + \omega_{-+} = 2(\omega_{xx} + \omega_{yy}). \quad (\text{E7})$$

Under the help of the Hellman-Feynman theorem, we have

$$\begin{aligned} \langle G | \sum_j S_j^z S_{j+1}^z | G \rangle &= \frac{\partial e_0}{\partial \Delta}, \\ \langle G | \sum_j (S_j^x S_{j+1}^x + S_j^y S_{j+1}^y) | G \rangle &= e_0 - \Delta \frac{\partial e_0}{\partial \Delta}. \end{aligned} \quad (\text{E8})$$

where e_0 is defined as

$$e_0 = \sum_j \langle G | (S_j^x S_{j+1}^x + S_j^y S_{j+1}^y + \Delta S_j^z S_{j+1}^z) | G \rangle. \quad (\text{E9})$$

The magnetic field h and magnetization m are related through the Legendre transform

$$h = \frac{1}{N} \frac{\partial e_0}{\partial m}. \quad (\text{E10})$$

Combining these results together, the first frequency moment sum rule can be expressed as

$$\begin{aligned} \omega_{+-}(q) + \omega_{-+}(q) &= -\frac{2}{N} \left[(\Delta(1 + \Delta \cos q) - 2 \cos q) \frac{\partial e_0}{\partial \Delta} \right. \\ &\quad \left. + (1 - \Delta \cos q) e_0 - m \frac{\partial e_0}{\partial m} \right], \end{aligned} \quad (\text{E11})$$

$$\omega_{zz}(q) = -\frac{1}{N} (1 - \cos q) \left(e_0 - \Delta \frac{\partial e_0}{\partial \Delta} \right). \quad (\text{E12})$$

APPENDIX F: BETHE EIGENSTATES AT SPECTRAL PEAK POSITIONS IN TRANSVERSE DSFS

In this section, we identify the Bethe eigenstates with the largest weight values around the spectral peaks at momenta $0, \frac{\pi}{2}, \pi$. The energies of these eigenstates can be obtained by solving the Bethe ansatz equations, which correspond to the peak positions in the DSSF spectra as shown in Fig. 5. In the following, $S_T^z = \sum_{i=1}^N S_i^z$ is the z component of the total spin, $M = \frac{N}{2} - S_T^z$ is the number of magnons, and $m = S_T^z/N$ is the magnetization per site. For simplicity, we assume that both N

and S_T^z are even integer numbers. For the expressions of the momentum k of the excitations $\chi^{(n)}$ ($n = 1, 2$), ψ , and ψ^* , the limit of $N \rightarrow \infty$ is taken with m fixed.

For the line of $\chi_{\pi/2}^{(3)}$ in Fig. 5, the Bethe quantum numbers of the corresponding Bethe eigenstate are given by

$$\begin{aligned} I^{(3)} &= \frac{1}{2} S_T^z, \\ I_j^{(1)} &= -\frac{M-4}{2} + j - 1 + \Theta\left(j - \frac{M}{2} + 3\right), \end{aligned} \quad (\text{F1})$$

where $1 \leq j \leq M-3$, and Θ is the step function defined as $\Theta(x) = 0$ if $x \leq 0$ and $\Theta(x) = 1$ if $x > 0$. The momenta of the excitations are determined by Eq. (B4) as $k_{\chi^{(3)}} = \pi(1-m)$, $k_{\psi} = 0$, and $k_{\psi^*} = \pi(1/2+m)$.

For the line of $\chi_{\pi/2}^{(2)}$, the Bethe quantum numbers of the corresponding Bethe eigenstate are

$$\begin{aligned} I^{(2)} &= -\frac{1}{2} S_T^z, \\ I_j^{(1)} &= -\frac{M-3}{2} + j - 2 + \Theta\left(j - \frac{M}{2} + 1\right), \end{aligned} \quad (\text{F2})$$

where $1 \leq j \leq M-2$. The momenta of the excitations are $k_{\chi^{(2)}} = \pi(1+m)$, $k_{\psi} = \pi$, and $k_{\psi^*} = \pi(3/2-m)$.

For the line of $\chi_{\pi/2}^{(2)}$, the Bethe quantum numbers of the corresponding Bethe eigenstate are

$$\begin{aligned} I^{(2)} &= S_T^z + 2, \\ I_j^{(1)} &= -\frac{M-3}{2} + j, \end{aligned} \quad (\text{F3})$$

where $1 \leq j \leq M-2$. The momenta of the excitations are $k_{\chi^{(2)}} = \pi(1-2m)$, $k_{\psi} = k_{\psi^*} = \pi(1/2+m)$.

For the line of $R_{\pi/2}^{+-}$ ($m \leq 1/4$), the Bethe quantum numbers of the corresponding Bethe eigenstate are

$$I_j^{(1)} = -\frac{M-1}{2} + j - 1 + \Theta\left(j - M + \frac{N}{4}\right), \quad (\text{F4})$$

where $1 \leq j \leq M$. The momenta of the excitations are $k_{\psi_1} = \pi(1/2+m)$ and $k_{\psi_2} = \pi(1-m)$.

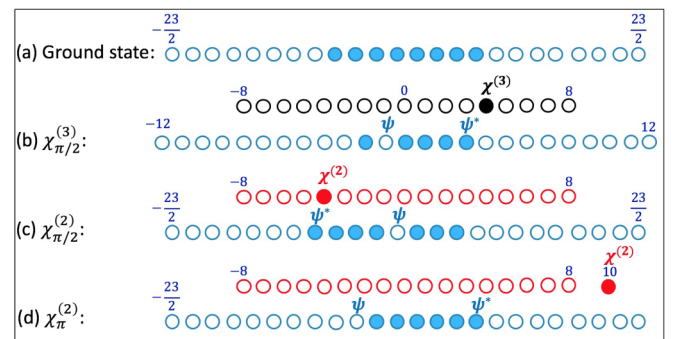


FIG. 9. Distributions of Bethe quantum numbers for the string excitations which have local maximal weight values at the corresponding momentum. The positions of the solid circles represent the Bethe quantum numbers of the particles. The system size and magnetization are taken as $N = 32$ and $S_T^z = 8$.

For the line of R_0^{+-} , the Bethe quantum numbers of the corresponding Bethe eigenstate are

$$I_j^{(1)} = -\frac{M-1}{2} + j, \quad 1 \leq j \leq M-1,$$

$$I_M^{(1)} = \frac{M-1}{2} + S_T^z + 1. \quad (\text{F5})$$

The momenta of the excitations are $k_\psi = \pi(1/2 + m)$ and $k_{\psi^*} = \pi(1/2 - m)$.

For the line of $R_{\pi/2}^{+-,a}$, the Bethe quantum numbers of the corresponding Bethe eigenstate are

$$I_j^{(1)} = -\frac{M-1}{2} + j, \quad 1 \leq j \leq M-1,$$

$$I_M^{(1)} = \frac{N}{4} - \frac{M-1}{2}. \quad (\text{F6})$$

The momenta of the excitations are $k_\psi = \pi(1/2 + m)$ and $k_{\psi^*} = \pi(1 - m)$.

For the line of $R_{\pi/2}^{+-,b}$, the Bethe quantum numbers of the corresponding Bethe eigenstate are

$$I_j^{(1)} = -\frac{M-1}{2} + j, \quad 1 \leq j \leq M-1,$$

$$I_M^{(1)} = \frac{N}{4} + \frac{M-1}{2}. \quad (\text{F7})$$

The momenta of the excitations are $k_\psi = \pi(3/2 - m)$ and $k_{\psi^*} = \pi m$. Schematically, we present the distributions of Bethe quantum numbers of string excitations in Fig. 9.

-
- [1] P. A. Deift and X. Zhou, *Commun. Math. Phys.* **165**, 175 (1994).
- [2] J. Sagi and I. Affleck, *Phys. Rev. B* **53**, 9188 (1996).
- [3] S. Sachdev and A. P. Young, *Phys. Rev. Lett.* **78**, 2220 (1997).
- [4] R. M. Konik, *Phys. Rev. B* **68**, 104435 (2003).
- [5] R. Coldea, D. A. Tennant, E. M. Wheeler, E. Wawrzynska, D. Prabhakaran, M. Telling, K. Habicht, P. Smeibidl, and K. Kiefer, *Science* **327**, 177 (2010).
- [6] S. Sachdev and B. Keimer, *Phys. Today* **64**(2), 29 (2011).
- [7] M. Ganahl, E. Rabel, F. H. L. Essler, and H. G. Evertz, *Phys. Rev. Lett.* **108**, 077206 (2012).
- [8] A. Imambekov, T. L. Schmidt, and L. I. Glazman, *Rev. Mod. Phys.* **84**, 1253 (2012).
- [9] T. Fukuhara, P. Schauss, M. Endres, S. Hild, M. Cheneau, I. Bloch, and C. Gross, *Nature (London)* **502**, 76 (2013).
- [10] J. Wu, M. Kormos, and Q. Si, *Phys. Rev. Lett.* **113**, 247201 (2014).
- [11] R. Vlijm and J.-S. Caux, *Phys. Rev. B* **93**, 174426 (2016).
- [12] L. S. Wu, W. J. Gannon, I. A. Zaliznyak, A. M. Tsvelik, M. Brockmann, J.-S. Caux, M. S. Kim, Y. Qiu, J. R. D. Copley, G. Ehlers, A. Podlesnyak, and M. C. Aronson, *Science* **352**, 1206 (2016).
- [13] M. Babadi, E. Demler, and M. Knap, *Phys. Rev. X* **5**, 041005 (2015).
- [14] N. Andrei, Quench dynamics in integrable systems, in *Strongly Interacting Quantum Systems out of Equilibrium*, edited by T. Giamarchi, A. J. Millis, O. Parcollet, H. Saleur, and L. F. Cugliandolo, Lecture Notes of the Les Houches Summer School Vol. 99 (Oxford University Press, Oxford, 2016).
- [15] H. Bethe, *Z. Phys.* **71**, 205 (1931).
- [16] C. N. Yang and C. P. Yang, *Phys. Rev.* **150**, 321 (1966).
- [17] C. N. Yang and C. P. Yang, *Phys. Rev.* **150**, 327 (1966).
- [18] E. K. Sklyanin, L. A. Takhtadzhyan, and L. D. Faddeev, *Theor. Math. Phys.* **40**, 688 (1979).
- [19] R. J. Baxter, *Exactly Solved Models in Statistical Mechanics* (Academic Press, London, 1982).
- [20] M. Takahashi, *Thermodynamics of One-dimensional Solvable Models* (Cambridge University Press, Cambridge, England, 1999).
- [21] X.-W. Guan, M. T. Batchelor, and C. Lee, *Rev. Mod. Phys.* **85**, 1633 (2013).
- [22] Y.-P. Wang, W.-L. Yang, J. Cao, and K. Shi, *Off-Diagonal Bethe Ansatz for Exactly Solvable Model* (Springer, Berlin, Heidelberg, 2015).
- [23] A. Bastianello and L. Piroli, *J. Stat. Mech.: Theory Exp.* (2018) 113104.
- [24] E. Ilievski, J. De Nardis, M. Medenjak, and T. Prosen, *Phys. Rev. Lett.* **121**, 230602 (2018).
- [25] J. De Nardis, D. Bernard, and B. Doyon, *Phys. Rev. Lett.* **121**, 160603 (2018).
- [26] M. Ljubotina, M. Znidaric, and T. Prosen, *Phys. Rev. Lett.* **122**, 210602 (2019).
- [27] S. Gopalakrishnan and R. Vasseur, *Phys. Rev. Lett.* **122**, 127202 (2019).
- [28] M. Karbach and G. Müller, *Phys. Rev. B* **62**, 14871 (2000).
- [29] D. Biegel, M. Karbach, and G. Müller, *Europhys. Lett.* **59**, 882 (2002).
- [30] J. Sato, M. Shiroishi, and M. Takahashi, *J. Phys. Soc. Jpn.* **73**, 3008 (2004).
- [31] J.-S. Caux and J. M. Maillet, *Phys. Rev. Lett.* **95**, 077201 (2005).
- [32] J.-S. Caux, R. Hagemans, and J. M. Maillet, *J. Stat. Mech.: Theory Exp.* (2005) P09003.
- [33] J.-S. Caux, *J. Math. Phys.* **50**, 095214 (2009).
- [34] M. Kohno, *Phys. Rev. Lett.* **102**, 037203 (2009).
- [35] J. Mossel and J.-S. Caux, *New J. Phys.* **12**, 055028 (2010).
- [36] W. Liu and N. Andrei, *Phys. Rev. Lett.* **112**, 257204 (2014).
- [37] N. Ishimura, and H. Shiba, *Prog. Theor. Phys.* **63**, 743 (1980).
- [38] H. Yoshizawa, K. Hirakawa, S. K. Satija, and G. Shirane, *Phys. Rev. B* **23**, 2298 (1981).
- [39] S. E. Nagler, W. J. L. Buyers, R. L. Armstrong, and B. Briat, *Phys. Rev. Lett.* **49**, 590 (1982).
- [40] S. E. Nagler, W. J. L. Buyers, R. L. Armstrong, and B. Briat, *Phys. Rev. B* **28**, 3873 (1983).
- [41] S. E. Nagler, D. A. Tennant, R. A. Cowley, T. G. Perring, and S. K. Satija, *Phys. Rev. B* **44**, 12361 (1991).
- [42] A. Zheludev, M. Kenzelmann, S. Raymond, E. Ressouche, T. Masuda, K. Kakurai, S. Maslov, I. Tsukada, K. Uchinokura, and A. Wildes, *Phys. Rev. Lett.* **85**, 4799 (2000).
- [43] M. B. Stone, D. H. Reich, C. Broholm, K. Lefmann, C. Rischel, C. P. Landee, and M. M. Turnbull, *Phys. Rev. Lett.* **91**, 037205 (2003).

- [44] Z. He, T. Taniyama, T. Kyōmen, and M. Itoh, *Phys. Rev. B* **72**, 172403 (2005).
- [45] S. Kimura, H. Yashiro, K. Okunishi, M. Hagiwara, Z. He, K. Kindo, T. Taniyama, and M. Itoh, *Phys. Rev. Lett.* **99**, 087602 (2007).
- [46] M. Mourigal, M. Enderle, A. Klopfferpieper, J.-S. Caux, A. Stunault, and H. M. Ronnow, *Nat. Phys.* **9**, 435 (2013).
- [47] Z. Wang, J. Wu, S. Xu, W. Yang, C. Wu, A. K. Bera, A. T. M. Nazmul Islam, B. Lake, D. Kamenskyi, P. Gogoi, H. Engelkamp, N. Wang, J. Deisenhofer, and A. Loidl, *Phys. Rev. B* **94**, 125130 (2016).
- [48] A. H. Bougourzi, M. Couture, and M. Kacir, *Phys. Rev. B* **54**, R12669(R) (1996).
- [49] A. Abada, A. Bougourzi, and B. Si-Lakhal, *Nucl. Phys. B* **497**, 733 (1997).
- [50] A. H. Bougourzi, M. Karbach, and G. Müller, *Phys. Rev. B* **57**, 11429 (1998).
- [51] J.-S. Caux, H. Konno, M. Sorrell, and R. Weston, *J. Stat. Mech.: Theory Exp.* (2012) P01007.
- [52] M. Jimbo and T. Miwa, *Algebraic Analysis of Solvable Lattice Models* (American Mathematical Society, Providence, 1995).
- [53] V. E. Korepin, N. M. Bogoliubov, and A. G. Izergin, *Quantum Inverse Scattering Method and Correlation Functions* (Cambridge University Press, Cambridge, England, 1993).
- [54] V. E. Korepin, *Commun. Math. Phys.* **86**, 391 (1982).
- [55] N. A. Slavnov, *Theor. Math. Phys.* **79**, 502 (1989).
- [56] J. M. Maillet and J. S. de Santos, *Am. Math. Soc. Trans.-Ser. 2* **201**, 137 (2000).
- [57] N. Kitanine, J. Maillet, and V. Terras, *Nucl. Phys. B* **567**, 554 (2000).
- [58] J. des Cloizeaux and J. J. Pearson, *Phys. Rev.* **128**, 2131 (1962).
- [59] Z. Wang, J. D. Wu, W. Yang, A. Kumar Bera, D. Kamenskyi, A. T. M. Nazmul Islam, S. L. Xu, J. Matthew Law, B. Lake, C. Wu, and A. Loidl, *Nature (London)* **554**, 219 (2018).
- [60] M. Karbach, D. Biegel, and G. Müller, *Phys. Rev. B* **66**, 054405 (2002).
- [61] R. Hagemans and J.-S. Caux, *J. Phys. A: Math. Theor.* **40**, 14605 (2007).
- [62] M. Pustilnik, M. Khodas, A. Kamenev, and L. I. Glazman, *Phys. Rev. Lett.* **96**, 196405 (2006).
- [63] R. G. Pereira, S. R. White, and I. Affleck, *Phys. Rev. Lett.* **100**, 027206 (2008).
- [64] P. C. Hohenberg and W. F. Brinkman, *Phys. Rev. B* **10**, 128 (1974).
- [65] O. Babelon, H. de Vega, and C. Viallet, *Nucl. Phys. B* **220**, 13 (1983).
- [66] F. Woynarovich, *J. Phys. A: Math. Gen.* **15**, 2985 (1982).
- [67] J. Mossel, Dynamics of the antiferromagnetic Heisenberg spin-1/2 chain, Master's thesis, University of Amsterdam, 2008.
- [68] J. Voit, *J. Phys.: Condens. Matter* **5**, 8305 (1993).
- [69] T. Fukuhara, A. Kantian, M. Endres, M. Cheneau, P. Schauss, S. Hild, D. Bellem, U. Schollwock, T. Giamarchi, C. Gross, I. Bloch, and S. Kuhr, *Nat. Phys.* **9**, 235 (2013).
- [70] N. Kitanine, J. Maillet, and V. Terras, *Nucl. Phys. B* **554**, 647 (1999).